Dynamic Response Analysis of Embankment Slopes Based on FLAC3D Simulation

Yichang Zhao [1,*], Dengchen Zhou [2]

[1] North China University of Water Resources and Electric Power, Zhengzhou, China, 450045

[2] School of Earth Sciences, Yunnan University, Kunming, China, 650500

* Corresponding Author Email: 15083156191@163.com

Abstract. The analysis of deformation and failure mechanisms of embankment slopes under seismic action is crucial for slope engineering design: this study uses FLAC3D to construct a slope model, simulating failure forms under Wolong (WL), Lushan (LS), and Luding (LD) seismic waves and innovatively examining dynamic response distributions of acceleration, displacement, and stress at different slope positions and effects of distinct seismic sequences. Results show that (1) under WL waves, the slope remains undamaged with more sensitive slope midpoint acceleration responses, where WL/LS waves induce two low-amplitude fluctuations while LD waves trigger a single concentrated fluctuation with abrupt changes; (2) the displacements at all points increase linearly with the load. Under the LD seismic waves, the slope displacement rises linearly after a brief fluctuation and reaches the largest peak; (3) stress decreases with elevation due to geometric dispersion but mid-slope stress is most sensitive, with LS waves inducing large-amplitude abrupt stress fluctuations and the highest peaks; (4) the slope midpoint shows the most pronounced responses in acceleration, displacement, and stress (followed by the base and crest), with LD waves posing the most significant threat to slope stability.

Key words: Embankment Slope, Dynamic Response, Seismic Sequence, Numerical Simulation

1. Introduction

Landslides triggered by seismic-induced slope instability pose severe risks to human safety and economic assets, often causing losses surpassing those directly inflicted by earthquakes themselves. For instance, on July 19, 2018, an extreme soil landslide in Taozi Township, Yanyuan County, Sichuan Province, destroyed nearly 400 meters of rural roads and blocked Taozigou, forming a dangerous quake lake with economic damages reaching approximately 13 million yuan [1]. On July 23, 2019, a 118,800 m³ landslide in Zhenxiong County, Yunnan Province, resulted in 44 fatalities across 18 households [2]. Another incident on March 15, 2019, in Xiangning County, Shanxi Province, caused 20 deaths, 13 injuries, and direct losses of 7.1348 million yuan [3]. These cases highlight the critical need for in-depth studies on deformation and failure mechanisms of embankment slopes under seismic loading, which holds significant theoretical and practical value for engineering design, maintenance, and disaster mitigation in seismically active regions.

Current methodologies for analyzing slope stability under seismic loading primarily adopt three approaches: 1) shaking table tests, 2) analytical solutions, 3) numerical simulations [4]. Dou Yanghao et al. [5] employed shaking table tests to design moderately steep bedding rock slopes with layer dip angles exceeding slope angles, investigating their dynamic responses and failure modes under unidirectional and coupled seismic excitations. Wang Runqing et al. [6] formulated mechanical equilibrium equations for free and coordinated rock deformation, proposing a framework to classify deformation types and assess overall slope stability, with programmed analysis of flexural toppling in anti-dip rock slopes via Matlab [6]. Chen Yongming et al. [7] utilized discrete element modeling with real seismic records to simulate instability mechanisms in jointed rock slopes, combining strength reduction methods to calculate seismic safety factors. Liu Shiqi et al. [8] adopted discrete element analysis to reveal the progressive collapse process of Hongshiyan slope at the mesoscopic scale, showing pronounced crack development in weak interlayers under seismic loads. Li Sixuan et al. [9] measured shear strength parameters through varied direct shear tests and used FLAC3D to

simulate stability changes under different shear conditions, analyzing mechanical effects of testing methods. Luo Gui et al. [10] integrated pseudo-dynamic and 3D Spencer limit equilibrium methods to develop a wave-effect-aware stability analysis framework, examining influences of geometric/soil parameters and wave characteristics on pseudo-dynamic/static safety factors.Although current research on slope stability under seismic action has been relatively systematic and comprehensive, investigations into the relationship between seismic wave propagation and slope response, as well as the effects of different seismic sequences on embankment slope damage, remain limited. Further in-depth studies are necessary to provide novel insights and more comprehensive analytical methods for evaluating slope stability under seismic loading.

This study employs FLAC3D software to simulate dynamic responses of embankment slopes under various seismic sequences, including acceleration, displacement, and stress responses. By systematically analyzing seismic wave input characteristics and integrating coupled wave-slope interaction mechanisms, this research establishes a holistic analytical framework that combines wave propagation in rock media with geomechanical responses of embankment slopes. This methodology enhances the comprehensiveness of stability assessments for slopes subjected to seismic excitation.

2. Model Configuration and Boundary Conditions

2.1. Model Geometry and Material Properties

2.1.1. Mesh Size Determination

According to Kuhlemeyer et al. [11], the spatial discretization in FLAC3D modeling must adhere to wavelength constraints governed by the maximum frequency component of seismic waves, specifically ensuring that the mesh size does not exceed one-tenth of the minimum wavelength. The critical relationship is expressed as:

$$\Delta l \leq \left(\frac{1}{10} - \frac{1}{8}\right)\lambda \tag{1}$$

$$\lambda = \frac{C_s}{f} \tag{2}$$

In this formula, Δl represents the mesh size, λ denotes the minimum wavelength of seismic waves, C_s is the shear wave velocity of seismic waves, and f corresponds to the maximum frequency of the input seismic waves.

2.1.2. Slope model size

The geometric configuration of the slope model and the arrangement of monitoring points are illustrated in the figure below. The model features a total base length of 80m, an overall height of 30m, and an underlying stratum with a thickness of 10m. As shown in Fig. 1, twenty-two monitoring points were strategically deployed to capture real-time dynamic responses, including acceleration, displacement, and stress magnitudes induced by seismic waves.

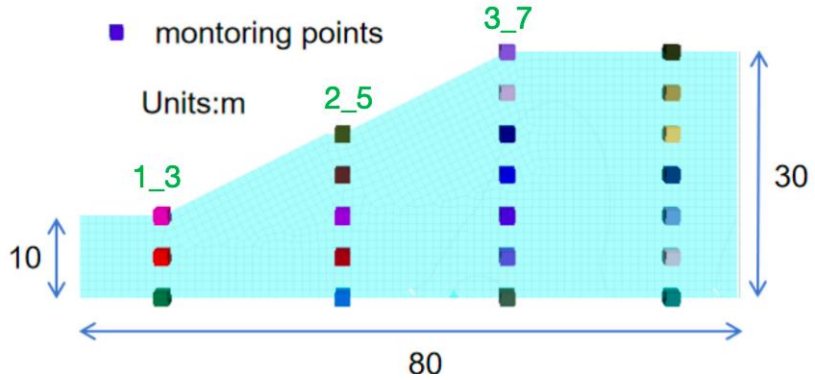

Fig. 1 Geometric Configuration and Monitoring Point Layout of the Slope Model

The slope model in this study adopts the Mohr-Coulomb constitutive relationship. The mechanical parameters of the constituent materials are comprehensively summarized in Table 1.

Table 1. Mechanical parameters of model materials

material parameter	density /(g/cm3)	modulus of elasticity /MPa	Poisson ratio	Internal friction Angle / (°)	cohesive /MPa
ground	2	500	0.3	25	0.03

2.2. Boundary conditions

In the numerical simulations, normal velocity constraints were imposed on the four lateral boundaries and the base of the model, restricting their normal velocities to zero, while the upper boundary remained unconstrained, thereby establishing fixed boundary conditions for static analysis of the slope model. Owing to computational limitations in simulating infinite or semi-infinite domains, the conventional fixed boundaries inevitably lead to wave reflection rather than transmission during seismic wave propagation, which fundamentally distorts the dynamic failure mechanisms observed under real earthquake loading conditions. To circumvent this limitation and approximate an infinite geological medium, the proposed modeling framework employs free-field boundary conditions for dynamic analysis. These boundaries are coupled with the main grid's lateral surfaces through viscous dampers, enabling effective transfer of unbalanced forces from the free-field grid to the primary model boundaries. This innovative coupling mechanism ensures efficient absorption of incident seismic waves at domain edges, thereby significantly improving the fidelity of slope dynamic response simulations under natural wave propagation conditions. The governing equation for the applied boundary forces is expressed as:

$$F_x = -\rho C_p\left(v_x^m - v_x^{ff}\right)A + F_x^{ff} \tag{3}$$

$$F_y = -\rho C_s\left(v_y^m - v_y^{ff}\right)A + F_y^{ff} \tag{4}$$

$$F_z = -\rho C_s\left(v_z^m - v_z^{ff}\right)A + F_z^{ff} \tag{5}$$

A represents the influence area of the free - field grid point. v_x^m, v_y^m, v_z^m denote the velocities in the corresponding directions on the side boundary of the main grid. v_x^{ff}, v_y^{ff}, v_z^{ff} represent the velocities in the corresponding directions on the connection boundary of the side free - field grid; F_x^{ff}, F_y^{ff}, F_z^{ff} signify the forces at the free - field stress grid points around the grid; C_p and C_s indicate the propagation velocities of compression waves and shear waves at the side boundary in the model medium.

2.3. Load seismic waves

The seismic waves used in this numerical simulation were extracted from actual ground motion records monitored in the Wolong (WL), Lushan (LS), and Luding (LD) regions of Wenchuan. Initial displacements and velocities of all grid points within the domain were reset to zero to eliminate pre-existing kinematic conditions. Subsequently, a gravitational acceleration of 10g was applied to the model to generate initial geostatic stresses, followed by five distinct acceleration loads along the xz-direction (ranging from 0.1g to 0.5g) within the spatial domain of (−0.1, 0.1) at the model base. Seismic waves corresponding to 0.1g acceleration levels from the WL, LS, and LD regions were sequentially applied, with durations of 7.5s, 10s, and 7s, respectively. The acceleration time histories for these waves are presented in Fig. 2, arranged from top to bottom as WL, LS, and LD.

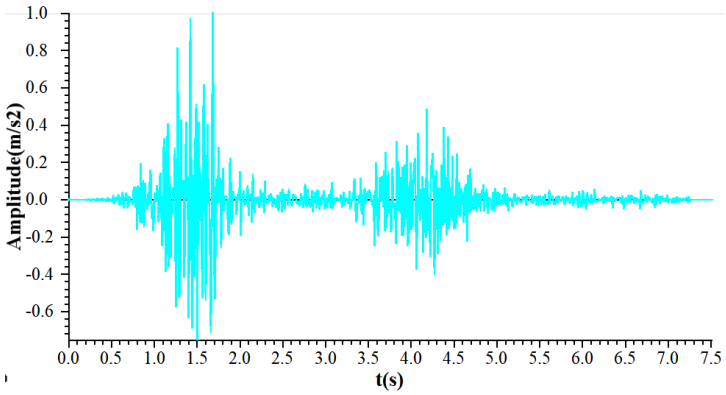

(a) WL seismic waves

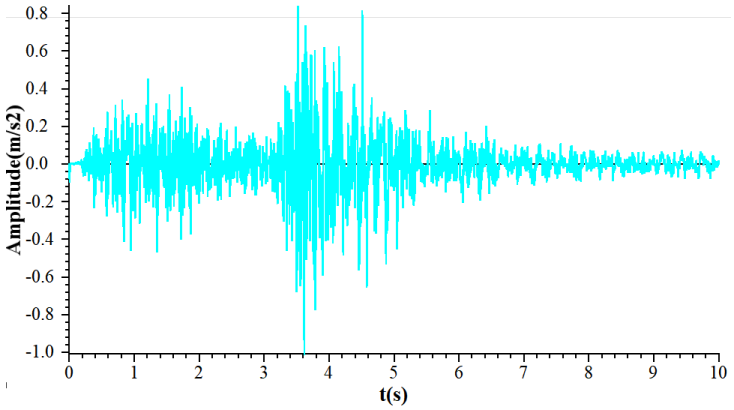

(b) LS seismic waves

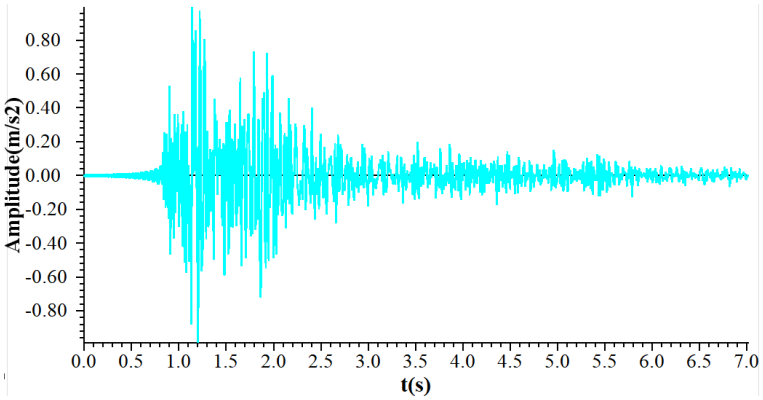

(c) LD seismic waves

Fig. 2 Acceleration time - history curves of three kinds of seismic waves

2.4. Damping Configuration

In FLAC3D dynamic analysis, three primary damping formulations are commonly employed: local damping, Rayleigh damping, and lagging damping. Local damping dissipates energy by introducing dampers in specific localized regions, a mechanism that operates on a relatively simple principle and is therefore particularly suitable for simplified models where computational efficiency and straightforward implementation are prioritized. It exhibits inherently frequency-insensitive characteristics, meaning its damping effect remains consistent across a broad spectrum of vibration frequencies without significant variation, which can be effectively considered as a form of frequency-independent damping that provides stable and reliable energy dissipation. Therefore, the simplified model adopted in this study utilizes local damping to balance accuracy and computational efficiency. The relationship between the local damping coefficient and the critical damping ratio is as follows:

$$\alpha_L = \pi D \tag{6}$$

In this formula, α_L represents the local damping coefficient, which is set to 0.157 in this model, while D denotes the critical damping ratio.

3. Numerical Processing and Analysis

This section applies acceleration loads ranging from 0.1g to 0.5g to three monitoring points (1_3, 2_5, and 3_7) along the upward-sloping face of the embankment using FLAC3D. By imposing different seismic sequences on these identical slope positions and systematically analyzing their acceleration, displacement, and stress response data, the study investigates the distribution patterns of slope dynamic responses under seismic waves and the influence of varying seismic sequences on slope stability.

3.1. Acceleration Data Processing and Analysis

3.1.1. Acceleration Responses at Distinct Slope Positions

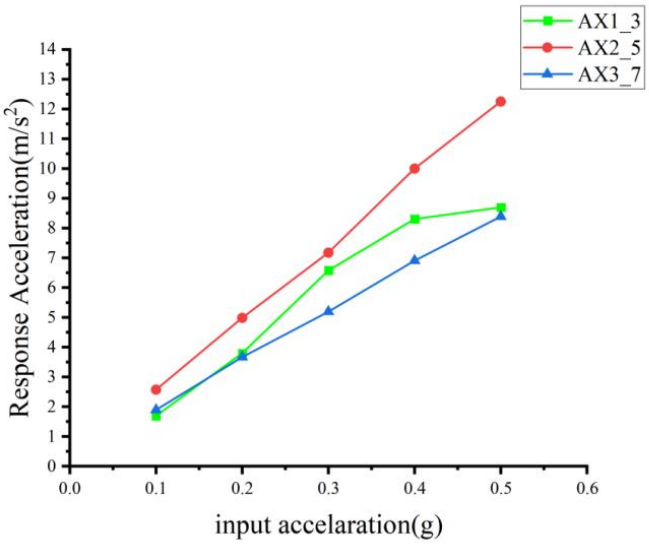

Fig. 3 Acceleration Response Curves at Monitoring Points under WL Seismic Waves

Three monitoring points (AX1_3, AX2_5, and AX3_7) along the upward-sloping face of the embankment, positioned in zones with unconstrained upper boundaries, were selected for acceleration response analysis. As illustrated in Fig. 3, the acceleration magnitudes at these points exhibit rapid and stable increases proportional to the applied acceleration loading. Linear regression analyses yield goodness-of-fit (R^2) values of 0.948, 0.999, and 0.999, respectively, confirming robust linear correlations. Under WL seismic waves with 0.5g acceleration loading, the accelerations at AX1_3, AX2_5, and AX3_7 reach 8.6938m/s², 12.2522m/s², and 8.387m/s², representing increases of 414.40%, 376.65%, and 343.63% compared to their 0.1g counterparts. These results demonstrate the significant influence of acceleration loading on response amplification and validate the structural integrity of the model during seismic excitation, as evidenced by stable wave propagation. Throughout the loading spectrum, AX2_5 consistently exhibits the highest acceleration magnitudes and steepest response gradients, followed by AX1_3 and AX3_7, indicating heightened sensitivity of the slope midpoint to WL wave inputs. This phenomenon is attributed to localized acceleration amplification caused by resonance effects between the slope structure and seismic waves, combined with constructive superposition of incident and reflected waves within the embankment. For practical engineering applications, targeted reinforcement of the slope midpoint is recommended. Notably, under 0.5g loading, the acceleration magnitude at AX2_5 exceeds that of AX3_7 by 3.8652m/s², highlighting significant spatial variability in dynamic response characteristics.

3.1.2. Acceleration Responses Under Different Seismic Sequences

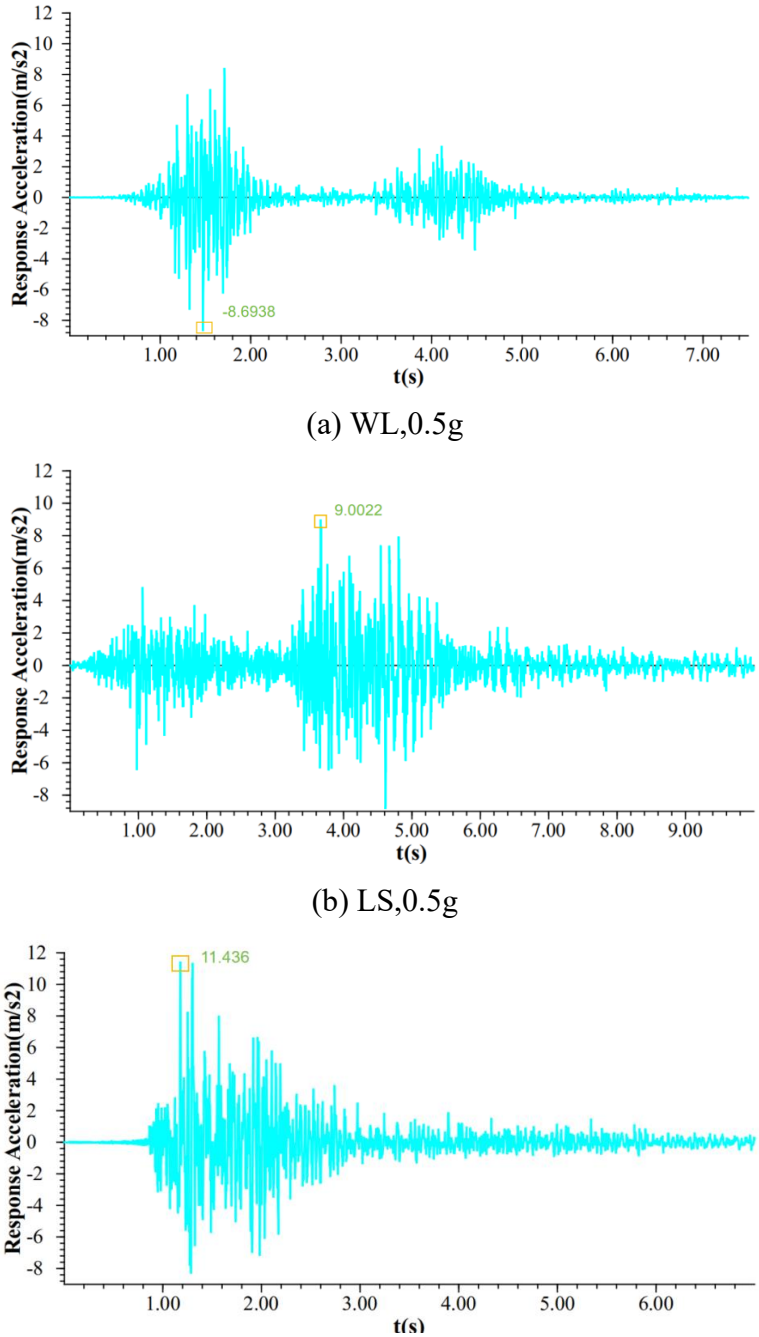

(a) WL,0.5g

(b) LS,0.5g

(c) LD,0.5g

Fig. 4 Acceleration Time Histories at Monitoring Point AX1_3 Under 0.5g Loading for Three Seismic Waves

As illustrated in Fig. 4, acceleration responses are observed at monitoring point AX1_3 under all three seismic waves (WL, LS, and LD) with 0.5g loading. Under WL waves, the acceleration waveform is concentrated within two intervals (0.8–2.4s and 3.4–5.0s), with the first interval exhibiting a gradual rise to a peak value of -8.6938m/s², followed by waveform stabilization after 5.0s. For LS waves, accelerations are predominantly activated between 0.2–5.4s, characterized by an abrupt transition to a peak of 9.0022m/s² at 3.8s and residual fluctuations persisting beyond 5.4s. Under LD seismic waves, the acceleration response waveform at AX1_3 is primarily concentrated within the time interval of 0.9s to 3.0s, exhibiting intense responses. The acceleration magnitude rapidly increases from 0 to a peak value of 11.436 m/s², with the waveform beginning to gradually contract at 1.6s. After 3.0s, the response gradually stabilizes, followed by minor post-stabilization oscillations. Acceleration

peaks under all three waves occur during early-to-mid excitation phases, with magnitudes ordered as LD > LS > WL. Under WL seismic waves, the slope acceleration responses manifest as two low-amplitude, short-duration fluctuations; under LS waves, they appear as a single concentrated fluctuation formed by dual-amplitude wave components; and under LD waves, they exhibit a single high-magnitude concentrated fluctuation with obvious abrupt changes. Under LD seismic waves, the slope exhibits more significant abrupt changes in acceleration response with higher peak values. In contrast, acceleration responses under WL and LS seismic waves are more gradual. For practical engineering applications, prioritized stabilization measures should be implemented for slopes subjected to LD seismic sequences.

3.2. Displacement Data Processing and Analysis

3.2.1. Displacement Responses at Distinct Slope Positions

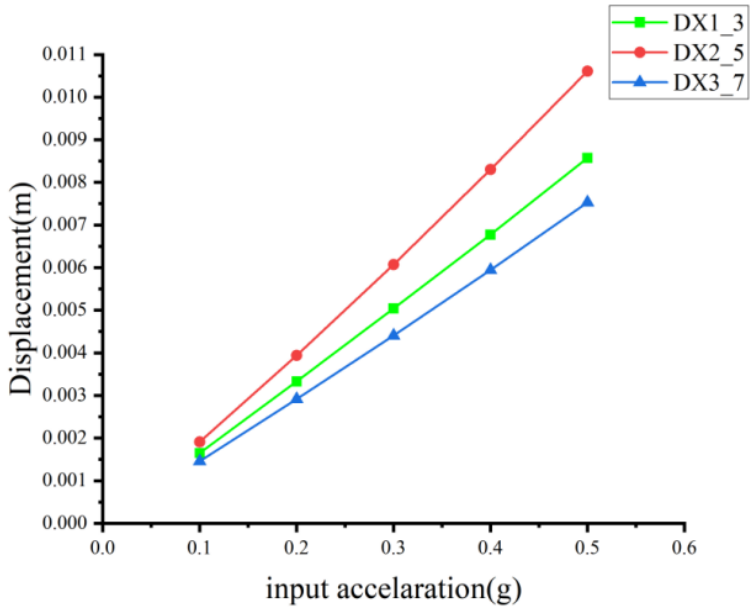

Fig. 5 Displacement Response Curves at Monitoring Points under LS Seismic Waves

As shown in Fig. 5, three monitoring points (DX1_3, DX2_5, DX3_7) at the same slope positions were selected to analyze displacements. The results show that displacements increase linearly and rapidly with the input acceleration. Under 0.5g loading, growth rates compared to 0.1g reach 419.39%, 455.50%, and 415.75% for the three points, respectively—indicating a pronounced effect of acceleration on displacement magnitude with consistent response patterns across all monitoring points. This suggests the slope model remained intact without failure throughout the process. DX2_5 consistently exhibited the largest displacement values with the steepest upward trend, followed by DX1_3 and DX3_7, highlighting that the slope midpoint (DX2_5) demonstrates the most sensitive and intense displacement response under LS seismic waves. For practical engineering applications, strict control and preventive measures should be prioritized at the slope midpoint to mitigate seismic risks.

3.2.2. Displacement Responses Under Different Seismic Sequences

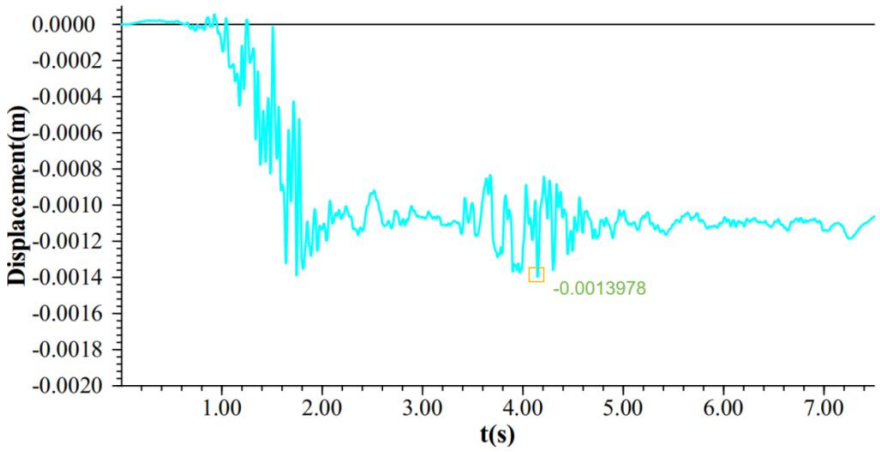

(a) WL,0.5g

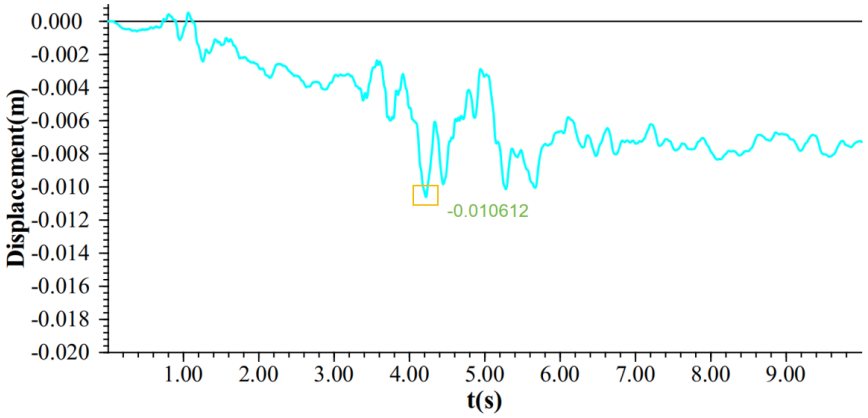

(b) LS,0.5g

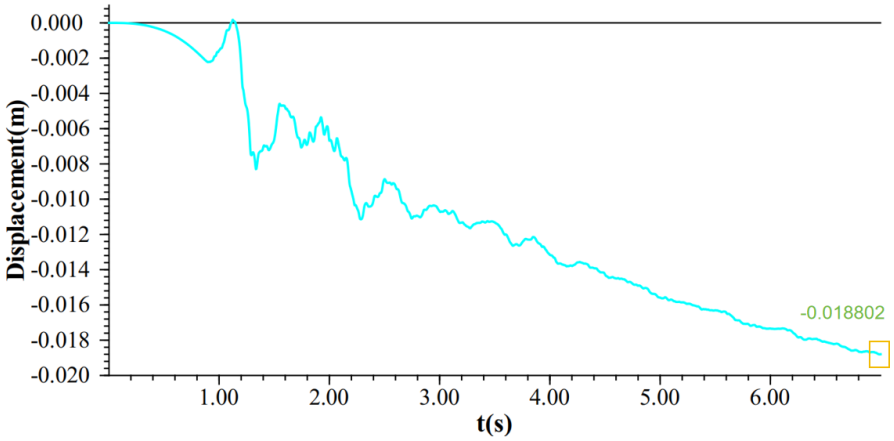

(c) LD,0.5g

Fig. 6 Displacement Time Histories at Monitoring Point DX2_5 Under 0.5g Loading for Three Seismic Waves

As shown in Fig. 6, the displacement response time-history plot of DX2_5 under WL seismic waves features dense fluctuations with an initial downward trend followed by stabilization, reaching a peak of -1.3978 mm. Under LS seismic waves, fluctuations are sparser, with overall displacements increasing through steady, gradual fluctuations without abrupt changes—the peak value here is -10.612 mm. For LD waves, DX2_5 displacement exhibits brief initial fluctuations followed by steady linear growth, culminating in a peak of -18.802 mm. The peak displacements follow the order LD > LS >

WL, with LS peaks accounting for 56.44% of LD values. This indicates that LD waves cause rapid slope destabilization and severe stability degradation, necessitating urgent reinforcement to prevent collapse and landslide under such sequences. In contrast, WL-induced displacements are negligible, with peak values only 7.43% of LD levels, confirming relative slope stability under WL seismic conditions.

3.3. Stress Data Processing and Analysis

3.3.1. Stress Responses at Distinct Slope Positions

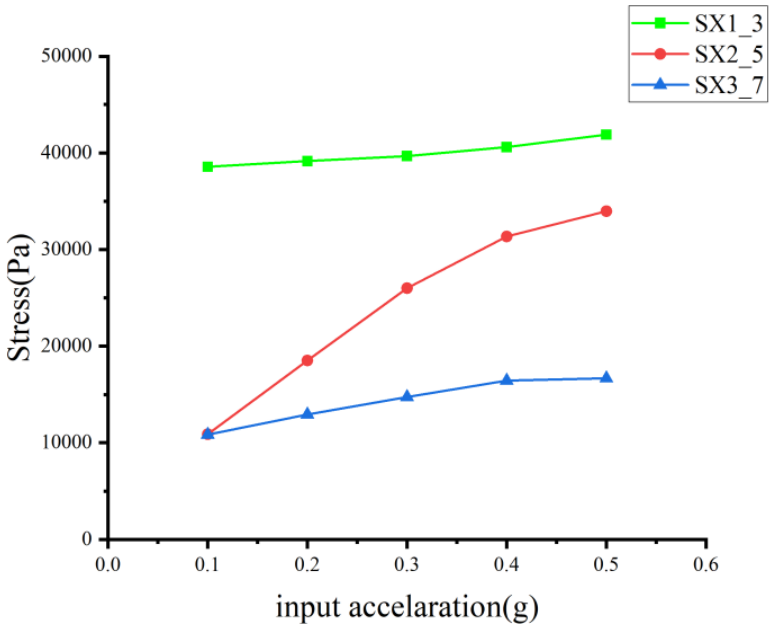

Fig. 7 Displacement Response Curves at Monitoring Points under LD Seismic Waves

As shown in Fig. 7, three monitoring points, SX1_3, SX2_5, and SX3_7, were set at the same positions as mentioned above to monitor the slope's stress. It can be seen from the figure that the stress values at these three points all increase as the input acceleration rises. Among them, the change trends of SX1_3 and SX3_7 are rather slow. The upward trend of SX2_5 is obvious between 0.1g and 0.3g and slows down relatively between 0.4g and 0.5g. This might be because the slope structure suffered a certain degree of damage under the action of 0.4g. In areas with strong seismic magnitudes, the stability of the slope mid - point is poor, so preventive reinforcement should be carried out at the slope mid - point. At 0.5g, the stresses at SX1_3, SX2_5, and SX3_7 increased by 8.63%, 211.89%, and 53.75% respectively compared with those at 0.1g. This indicates that the stress value at the slope mid - point under LD seismic waves is more sensitive to the acceleration load, while the responses at the slope base and crest are relatively weaker. Among them, the stress value of SX1_3 remains the largest throughout the process, followed by SX2_5 and then SX3_7. The higher the position, the smaller the stress value. This may be due to the attenuation caused by the geometric dispersion of stress during its propagation. It also shows that the effect of seismic waves on the slope stress varies greatly at different points on the slope.

3.3.2. Stress Responses Under Different Seismic Sequences

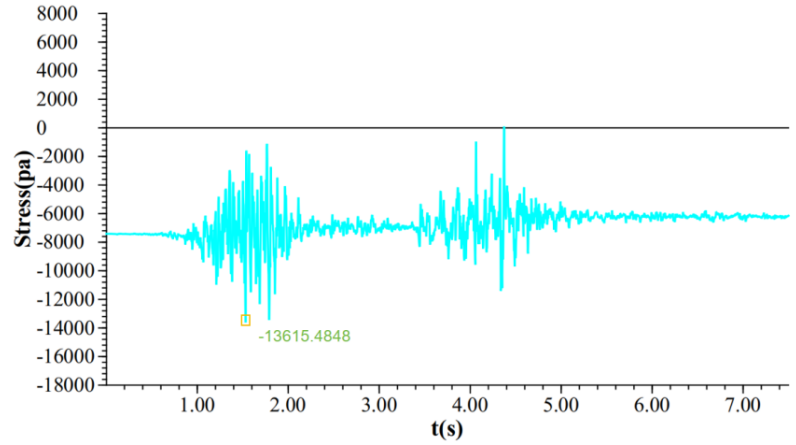

(a) WL,0.5g

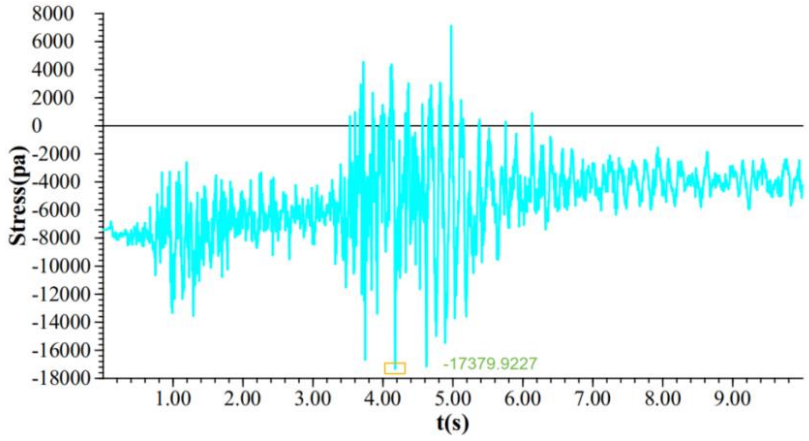

(b) LS,0.5g

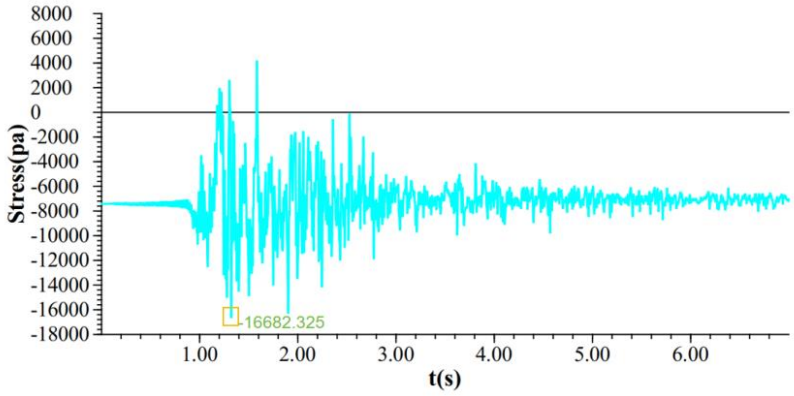

(c) LD,0.5g

Fig. 8 Stress Time Histories at Monitoring Point SX3_7 Under 0.5g Loading for Three Seismic Waves

As shown in Fig. 8, the stress response plot of SX3_7 under 0.5g loading for different seismic waves indicates: Under WL waves, SX3_7 experiences two stress fluctuations of similar amplitude, gradually increasing from the initial stress to a peak of -13615.4848 Pa. For LS waves, stress fluctuations concentrate between 3.4 s and 6.4 s, with amplitude abruptly increasing at 3.0 s before reaching -17379.9227 Pa. LD waves induce concentrated fluctuations between 0.9 s and 2.8 s, rapidly escalating from the initial stress to a peak of -16682.325 Pa. In terms of peak magnitude, LS waves generate the largest SX3_7 stress peak (LD peaks are close, while WL differs significantly). In terms of energy-

release duration, LS waves have the longest concentrated action time, followed by WL and LD. In terms of action form, both LS and LD waves cause large-amplitude abrupt changes, highlighting their substantial impact on slope stress distribution and the most obvious destabilization effects. These results indicate that LS and LD seismic sequences significantly alter slope stress states, posing notable risks to slope stability.

4. Research Findings

Through FLAC3D numerical simulation experiments, this study analyzes the dynamic response of slopes under different seismic sequences, with the main research results as follows:

(1) In terms of acceleration response, the slope did not suffer obvious damage under WL seismic waves. The acceleration magnitude increases with the continuous increase of acceleration load, showing a high goodness-of-fit and obvious linear change; due to the resonance effect and wave superposition, the acceleration response at the slope midpoint is more sensitive. The response acceleration at the slope midpoint (AX2_5) has always been the largest, reaching a peak of 12.2522 m/s^2 under 0.5g loading, with the most significant upward trend, followed by the slope base (AX1_3) and the slope crest (AX3_7); the acceleration of the slope under the three seismic waves all reaches the peak in the early to middle stage, and the numerical values are in the order of LD, LS, and WL.

(2) In terms of displacement response, the displacement at each point shows a linear increase trend with the acceleration load. The displacement at the slope midpoint is the largest and changes the fastest. Under the 0.5g acceleration load, the displacements at the slope base, midpoint, and crest are 8.57 mm, 10.61 mm, and 7.53 mm respectively; the displacement of the slope under LD seismic waves rises linearly, reaching the largest peak value of -18.802 m, followed by LS and WL. The peak value of the slope displacement under WL seismic waves is only 7.43% of that under LD waves, indicating that WL has little influence on the slope displacement and the slope is relatively stable under this seismic sequence.

(3) In terms of stress response, geometric dispersion of stress leads to smaller stress values at higher slope positions. The slope base (SX1_3), midpoint (SX2_5), and crest (SX3_7) have increased by 8.63%, 211.89%, and 53.75% respectively compared with 0.1g, with the stress response at the slope midpoint being more sensitive and the changes at the slope top and base being relatively insignificant. Under the action of 0.4g, the slope structure undergoes a certain degree of damage, leading to a slowdown in the response trend at the slope midpoint, which indicates that in areas with strong seismic magnitude, the stability of the slope midpoint is poor, and preventive reinforcement should be carried out at the slope midpoint; LS waves have a longer energy release time, a larger amplitude of abrupt stress changes in the slope, and cause the largest peak value of slope stress response.

5. Conclusions

(1) Under seismic waves, the slope midpoint exhibits the most pronounced responses in acceleration, displacement, and stress, being the most sensitive to seismic effects, followed by the slope base and then the crest. In practical engineering, this indicates that different slope positions should be treated with varying degrees of intervention: the midpoint requires prioritized support and reinforcement to mitigate the strong seismic impact on this region.

(2) Under WL seismic waves, slope acceleration responses manifest as two low-amplitude, short-duration fluctuations; LS waves induce a single concentrated fluctuation composed of dual-amplitude components; and LD waves trigger a single concentrated fluctuation with obvious abrupt changes. In terms of acceleration, displacement, and stress responses, LD waves generate the highest peak values, largest abrupt amplitude changes, and most rapid destabilization, posing the greatest threat to slope stability. Therefore, engineering measures must prioritize prevention and mitigation for slopes subjected to LD-type seismic sequences.

(3) There is a clear linear relationship between slope response magnitudes and the input seismic acceleration load. As the load increases, both acceleration and displacement responses rise rapidly. For stress responses, mid-slope stresses increase significantly, while growth rates at the crest and base are relatively slow. This allows for tailored protective measures at different slope positions corresponding to varying seismic intensity levels.

References

[1] Zhang Yixi, Zhao Cheng, Li Qingchun, et al. Characteristics and Genetic Mechanism of the '7.19' Extreme Landslide in Taozi Township, Yanyuan County, Sichuan Province [J]. Water Resources and Hydropower Engineering, 2023, 54(11): 181-191.

[2] Chen Ningsheng, Wu Mingyang, Li Anhui, et al. Investigation of the '1·22' Landslide Disaster in Zhenxiong County, Yunnan Province [J]. Mountain Research, 2024, 42(3): 422-430, 333.

[3] Qiu Daiping. Cause Analysis of the '3.15' Landslide in Xiangning County, Linfen City [J]. Natural Resources of North China, 2022(4): 126-129.

[4] Li Mei, Wu Jindong, Wang Di, et al. Study on Large Deformation and Instability Failure Modes of Slopes under Earthquake Loads [J]. Journal of Hunan University (Natural Sciences Edition), 2024, 51(09): 122-132.

[5] Dou Yanghao, Zhao Qihua, Zheng Xiuhong. Dynamic Response Characteristics and Failure Modes of Moderately Steep Bedding Rock Slopes under Earthquake Action [J]. China Earthquake Engineering Journal, 2025, 47(02): 393-403.

[6] Wang Runqing, Chen Congxin, Zheng Yun, et al. Stability Analysis Method for Flexural Toppling of Anti-Dip Rock Slopes under Earthquake Considering Deformation Coordination [J]. Chinese Journal of Rock Mechanics and Engineering, 2024, 43(01): 146-156.

[7] Chen Yongming, Teng Guangliang, Shi Yucheng, et al. Discrete Element Simulation of Slope Instability Mechanism of Baocheng Railway Tunnel 109 under Earthquake [J]. Chinese Journal of Geotechnical Engineering, 2013, 35(S1): 23-32.

[8] Liu Shiqi, Wang Huanling, Cheng Zhichao, et al. Discrete Element Analysis of Dynamic Response of Rock Slope Instability under Earthquake [J]. Chinese Journal of Geotechnical Engineering, 2023, 45(S2): 253-257.

[9] Li Sixuan, Zhang Xiaoming, Zhao Yi, et al. Influence of Direct Shear Test Methods on Stability of Benggang (Gully Erosion) Soil Slopes [J]. Research of Soil and Water Conservation, 2025, 32(03): 180-187.

[10] Luo Gui, Wan Yukuai, Liang Jinhang, et al. Three-Dimensional Limit Equilibrium Spencer Method for Pseudo-Dynamic Seismic Slope Stability Analysis [J]. Journal of Hebei University of Engineering (Natural Science Edition), 2025, 42(01): 58-65.

[11] L. R. K., John L. Finite Element Method Accuracy for Wave Propagation Problems [J]. Journal of the Soil Mechanics and Foundations Division, 1973, 99(5).